Inorganic Chemistry
Cite This: Inorg. Chem. XXXX, XXX, XXX–XXX
Article
pubs.acs.org/IC

Synthetic Iron Porphyrins for Probing the Differences in the Electronic Structures of Heme a_3, Heme d, and Heme d_1

Sk Amanullah, Paramita Saha, Rajat Saha, and Abhishek Dey*

Department of Inorganic Chemistry, Indian Association for the Cultivation of Science, Kolkata 700032, India

Supporting Information

ABSTRACT: A variety of heme derivatives are pervasive in nature, having different architectures that are complementary to their function. Herein, we report the synthesis of a series of iron porphyrinoids, which bear electron-withdrawing groups and/or are saturated at the β-pyrrolic position, mimicking the structural variation of naturally occurring hemes. The effects of the aforementioned factors were systematically studied using a combination of electrochemistry, spectroscopy, and theoretical calculations with the carbon monoxide (CO) and nitric oxide (NO) adducts of these iron porphyinoids. The reduction potentials of iron porphyrinoids vary over several hundreds of millivolts, and the X−O (X = C, N) vibrations of the adducts vary over 10−15 cm^{-1}. Density functional theory calculations indicate that the presence of electron-withdrawing groups and saturation of the pyrrole ring lowers the π^*-acceptor orbital energies of the macrocycle, which, in turn, attenuates the bonding of iron to CO and NO. A hypothesis has been presented as to why cytochrome c containing nitrite reductases and cytochrome cd_1 containing nitrite reductases follow different mechanistic pathways of nitrite reduction. This study also helps to rationalize the choice of heme a_3 and not the most abundant heme b cofactor in cytochrome c oxidase.

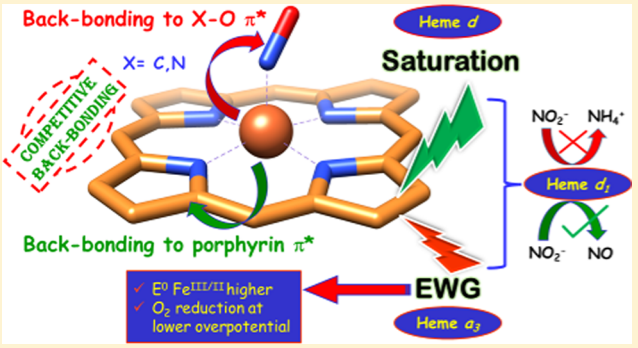

INTRODUCTION

Tetrapyrrole macrocycles are ubiquitous in nature and are known to play a central role in most living organisms.[1] Their importance stems from the unique attributes of tetrapyrroles for diverse bioenergetic processes by the versatility, concision, and molecular logic of the tetrapyrrole biosynthetic pathway.[2] All naturally occurring corrinoid, porphyrin, and (bacterio)-chlorin macrocycles, collectively known as the pigments of life, investigated so far are biosynthetically derived from uroporphyrinogen III.[3] In higher plants, tetrapyrrole synthesis occurs in plastids, where it is initiated by reduction of the glutamyl moiety of glutamyl-tRNA to glutamate-1-semi-aldehyde (Scheme 1).[4,5] Intermolecular transamination of glutamate semialdehyde generates 5-aminolevulinic acid (ALA), which is then transformed into uroporphyrinogen III, by the catalytic activity of ALA dehydratase, hydroxymethylbi-lane synthase, and uroporphyrinogen III synthase (Scheme 1).[5−8] Uroporphyrinogen III represents the first branch point in the pathway because methylation of this intermediate leads to the formation of siroheme, vitamin B_{12}, and cofactor F_{430}, whereas decarboxylation leads toward heme and chlorophyll synthesis.[3]

Although these porphyrinoids (porphyrins and porphyrin-like macrocycles) have similar biosynthetic pathways, they play distinctly different roles.[12] Hemes (iron-bound protoporphyrin IX) are commonly involved in a variety of biological transformations using molecular O_2, ranging from O_2 transport to substrate oxidation using high-valent (oxoferryl heme) intermediates.[13] Sirohemes (iron-bound isobacteriochlorin) catalyze the reduction of nitrite[14,15] and sulfite;[16,17] cyto-chrome cd_1 is also involved in nitrite reduction.[14,18,19] Heme d (iron-bound chlorin) is present in some catalases and peroxidases.[19−21] In prokaryotes (mainly in pathogenic bacteria), cytochrome bd have distinct physiological roles as terminal oxidases.[22] This clearly demonstrates the structure-dependent reactivity relationship of porphyrin and porphyrynoid macrocycles that is elegantly present in nature and is yet to be understood. For example, multi-c-heme-containing nitrite reductases (CcNiR) are known to be involved in dissimilatory nitrite reduction to ammonium ion and siroheme-containing nitrite reductases (CSNiR) are also known to be involved in assimilatory nitrite reduction to ammonium ion, while heme c and d_1 containing nitrite reductases (Cd_1NiR) are involved in dissimilatory nitrite reduction to nitric oxide (Figure 1B,C).[14,19] In cytochrome c oxidase (CcO) active site, a different kind of heme, heme a_3 (which contains electron-withdrawing formyl and hydroxyfarnesyl groups), is present in the O_2 binding site (Figure 1A). Recently, the Lu group has demonstrated how the reduction potential of heme in a functional model of CcO in myoglobin can be tuned up to ~215 mV.[23] The reason(s) for the different reactivities of these

Received: July 21, 2018

DOI: 10.1021/acs.inorgchem.8b02063
Inorg. Chem. XXXX, XXX, XXX–XXX

Scheme 1. Schematic Diagram of the Biosynthetic Pathways of Naturally Occurring Porphyrinoids[3]

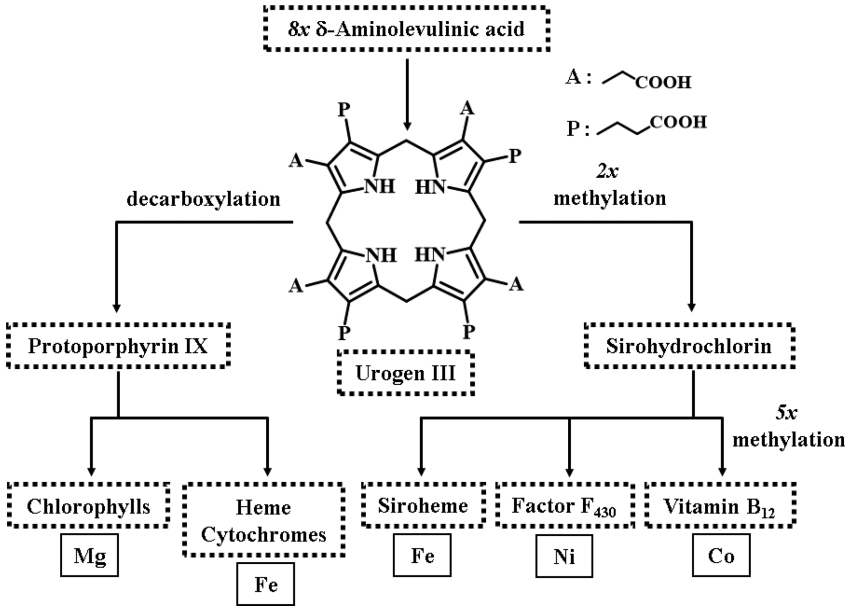

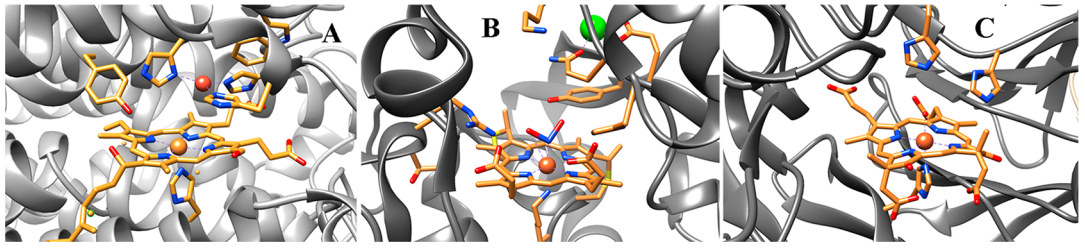

Figure 1. Crystal structure of the enzyme active sites. (A) CcO, which contains heme a_3 in the oxygen binding site (PDB 1OCR).[9] (B) Nitrite-bound pentaheme cytochrome *c* nitrite reductase, which contains heme *c* in the nitrite binding site (PDB 2E80).[10] (C) Cytochrome cd_1 nitrite reductase, which contains heme d_1 in the nitrite binding site (PDB 1NIR).[11] The structures have been redrawn using *Chimera 1.2rc* software.

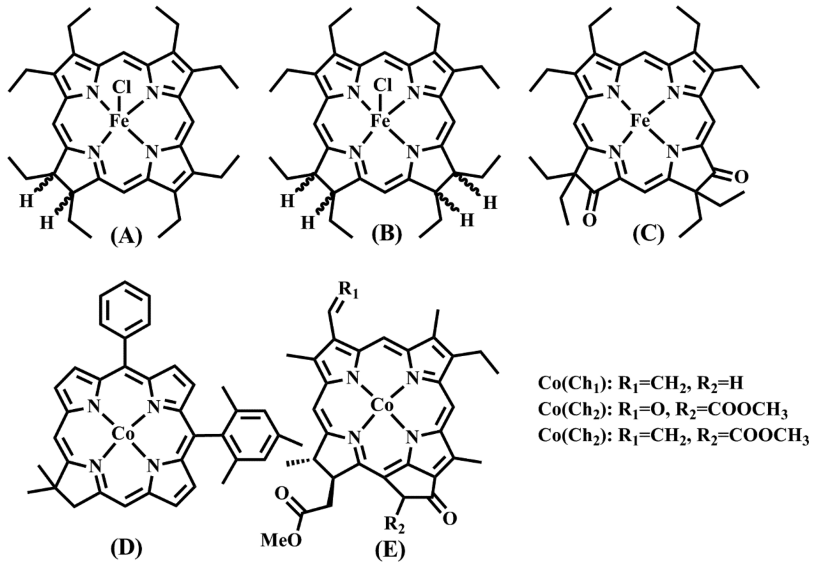

Figure 2. Representative molecules having saturated pyrrole centers: (A) Fe(OEC)Cl; (B) Fe(OEiBC)Cl.[29] (C) Heme d_1 mimic reported by Fujii et al.[37] (D) Cobalt chlorin reported by Nocera et al.[35] (E) Cobalt chlorins reported by Fukuzumi et al.[38]

enzymes is (are) still obscured. In the 1980s, a few groups had attempted to understand the effect of saturating the pyrrole rings by synthetic modeling and computational studies.[24−27] Holm and co-workers had synthesized reduced porphyrins like iron octaethylchlorin (FeOEC; Figure 2A) and iron octaethylisobactriochlorin (FeOEiBC; Figure 2B) by hydrogenation of their unsaturated analogues.[25,28−30] They were successful in attaching an isobacteriochlorin analogue to an

DOI: 10.1021/acs.inorgchem.8b02063
Inorg. Chem. XXXX, XXX, XXX−XXX

iron−sulfur cluster, resulting in a synthetic mimic of the Siroheme sulfite reductase active site.[31] However, these complexes are very unstable and are readily oxidized back to iron octaethylporphyrin (FeOEP) and did not even sustain routine ^{1}H NMR experiments.[29] Albeit the seminal work by Holm and co-workers, iron chlorins have not been investigated in detail and, unfortunately, most of the effort in this area is limited to a few groups, and further development in understanding the role of the structural variations in porphyrinoids awaits. Their abundance in the active sites of metalloenzymes involved in the sulfur and nitrogen cycle and some peroxidases compelled further research in trying to understand their electronic structure and reactivity. Wei and Ryan have reported nitric oxide (NO) complexes of FeOEP, where pyrrole rings are oxidized to pyrrolidone and the NO stretches of the complexes were lowered by 6−8 cm^{-1}.[32] Recently, Fukuzumi and co-workers[33,34] (Figure 2E) and Nocera and co-workers[35] (Figure 2D) have used cobalt and nickel chlorin for water splitting, renewing interest in these arcane macrocycles and their potential reactivities. The Bröring group reported porphyrins with one saturation at the meso position, forming isoporphyrin.[36] Fujii et al. reported a model for heme d_1 in cytochrome cd_1 nitrite reductase by varying keto groups attached with the porphyrin.[37]

In this Article, a convenient method has been designed to make stable iron chlorin analogues using a 1,3-cycloaddition reaction to form C−C bonds akin to the role of methyl transferases in biosynthetic pathways to form saturated porphyrins.[3] Both β-H's of one of the four pyrroles are replaced by ester groups for two reasons. First, this allows regioselective 1,3-cycloaddition reaction (due to the attachment of electron-withdrawing ester groups) with an azomethine ylide, and, second, it gives a good opportunity to probe the electronic structure of an iron porphyrin by introducing two electron-withdrawing groups. This can be directly correlated with heme a_3, which has two electron-withdrawing groups at the two β positions of the heme in the active site of CcO to reduce oxygen to water (Figure 1A). The pyrrole with ester groups is saturated to model heme d_1, which is saturated and contains electron-withdrawing groups (Figure 1C).[11] The effect of these peripheral modifications on the electronic structures of iron porphyrinoids is probed by employing their NO and carbon monoxide (CO) adducts.

EXPERIMENTAL DETAILS

Materials. All reagents used are of the highest grade commercially available. Iodine, trifluoroacetic acid, 2,3-dichloro-5,6-dicyano-1,4-benzoquinone, ethanol, aqueous ammonia solution, ceric ammonium nitrate (CAN), and sarcosine were purchased from Spectrochem Ltd. Diethyl ether, tetrahydrofuran (THF), acetonitrile (ACN), dichloromethane (DCM), and toluene were purchased from Rankem Ltd. Paraformaldehyde, anhydrous ferrous bromide ($FeBr_2$), 2,4,6-collidine, tetrabutylammonium perchlorate (TBAP), potassium hexafluorophosphate (KPF_6), and all buffers were purchased from Sigma-Aldrich Chemical Company. Methanol (MeOH) was purchased from Finar Limited as a solution for Leishman Stain. Sodium sulfate (Na_2SO_4) and zinc acetate [$Zn(OAc)_2{\cdot}2H_2O$] were purchased from Merck and used without any further purification. Unless otherwise mentioned, all reactions were performed at room temperature. Column chromatography was performed with silica gel (mesh size: 60−100, 100−200, and 230−400), basic alumina, and neutral alumina. NMR and electron paramagnetic resonance (EPR) tubes were purchased from Wilmad-LabGlass. THF was dried using potassium metal in the presence of benzophenone, until the color of the solution turned intense bluish green. Toluene was dried using sodium metal in the presence of benzophenone, until the color of the solution turned intense blue. MeOH was first dried as toluene using sodium after that it was distilled from magnesium cake.

Instrumentation. All electrochemical experiments were performed using a CH Instruments (model CHI710D electrochemical analyzer). Biopotentiostat reference electrodes were purchased from CH Instruments. The absorption spectra were measured in the Shimadzu spectrograph (UV-2100). The aerobic and anaerobic cuvettes were purchased from Starna Scientific. The Fourier transform infrared (FTIR) data were measured on a Shimadzu FTIR 8400S instrument. The KBr windows for IR spectroscopy were purchased from Sigma-Aldrich. The anaerobic setup for IR spectroscopy was purchased from PerkinElmer. All of the NMR spectra were recorded on a Bruker DPX-300, a Bruker DPX-400, or a DPX-500 spectrometer at room temperature. The mass spectrometry (MS) spectra are recorded by a QTOF Micro YA263 instrument. The EPR spectra were recorded on a X-band JEOL (JES FA200) instrument. Single-crystal X-ray diffraction (SCXRD) data were collected at 120 K using radiation on a SMART APEX diffractometer equipped with a CCD area detector with a graphite monochromator and Mo Kα (λ = 0.7107 Å) radiation. The structures were solved by the Patterson method, followed by successive Fourier and difference Fourier synthesis. Full-matrix least-squares refinements were performed on F^2 using *SHELXL-97* with anisotropic displacement parameters for all non-hydrogen atoms. The hydrogen atoms were refined isotropically, and their locations were determined from a difference Fourier map. All calculations were carried out using *SHELXL 97*,[39] *SHELXS 97*,[40] *PLATON 99*,[41] *ORTEP-32*,[42] and *WinGX system v1.64*.[43]

Synthesis. The porphyrins diester porphyrin (DEsP)[44,45] and tetraphenylporphyrin (TPP)[46] were prepared following reported procedures. The porphyrins were saturated using a 1,3-cycloaddition reaction to get the chlorins, i.e., diester chlorin (DEsC) and tetraphenylchlorin (TPC), respectively.

FeDEsP. To a solution of DEsP (50 mg, 0.082 mmol) in 20 mL of dry degassed THF was added 2,4,6-collidine (21 μL, 0.164 mmol), and the solution was stirred for 10 min in a glovebox. $FeBr_2$ (70 mg, 0.328 mmol) was added and the solution stirred overnight. The reaction mixture was worked up with dilute HCl, followed by the addition of DCM. The organic layer was washed with a brine solution and collected. It was dried over anhydrous Na_2SO_4 and purified by column chromatography with silica gel (60−120 mesh size) using a 1% MeOH/DCM mixture as the eluent. Yield: 90 ± 2% (45 ± 5 mg).

λ_{max} (DCM, nm): 412, 575, 612. ^{1}H NMR ($CDCl_3$): δ 82.53, 80.51, 76.34 (paramagnetic shift for β-pyrrolic ^{1}H's and meso ^{1}H's of Fe^{III}-HS complex). ESI-MS (positive-ion mode, MeOH): m/z 659.9 (45%; [M − H]$^+$). EPR (1 mM sample in dry THF, 4 K): an axial signal with g values of 5.88 and 1.97 (Figure S29). Anal. Calcd for $C_{38}H_{28}FeN_4O_4Cl$: C, 65.58; H, 4.06; N, 8.05. Found: C, 64.93; H, 4.44; N, 8.02 (FeDEsPCl, 0.5H_2O).

ZnDEsP. To a solution of DEsP (50 mg, 0.082 mmol) in 20 mL of dry THF was added $Zn(OAc)_2{\cdot}2H_2O$ (60 mg, 0.328 mmol), and and the solution was stirred for 3 h at room temperature. The reaction mixture was worked up with water, followed by the addition of DCM. The organic layer was washed with a brine solution and collected. It was dried over anhydrous Na_2SO_4 and purified by column chromatography with silica gel (60−120 mesh size) using a 1% MeOH/DCM mixture as the eluent. Yield: 90 ± 5% (50 ± 5 mg). The complex was crystallized by layering hexane over a solution in DCM. The crystal data are given below.

λ_{max} (DCM, nm): 422, 517, 551, 595. ^{1}H NMR ($CDCl_3$): δ 1.00 (t, 6H), 3.83 (q, 4H), 7.80 (m, 6H), 8.27 (d, 4H), 8.96 (s, 2H), 9.03 (d, 2H), 9.27 (d, 2H), 9.69 (s, 2H). ^{13}C NMR ($CDCl_3$, 100 MHz): δ 13.94, 61.41, 105.93, 120.72, 126.82, 127.69, 131.58, 132.63, 132.90, 133.73, 134.80, 142.29, 142.90, 150.05, 151.76, 152.24, 165.58. ESI-MS (positive-ion mode, ACN): m/z 668.5 (40%; [M]$^+$), 690.5 (100%; [M + Na]$^+$).

DEsC. Paraformaldehyde (0.1 g, 3.3 mmol) and *N*-methylglycine (0.11g, 1.32 mmol) were taken in a 25 mL two-neck round-bottomed flask equipped with a condenser attached with a Schlenk line. A total of 5 mL of dry THF was added and refluxed for 20 min until an off-

DOI: 10.1021/acs.inorgchem.8b02063
Inorg. Chem. XXXX, XXX, XXX−XXX

Scheme 2. Synthetic Strategy of the Porphyrins and Chlorins

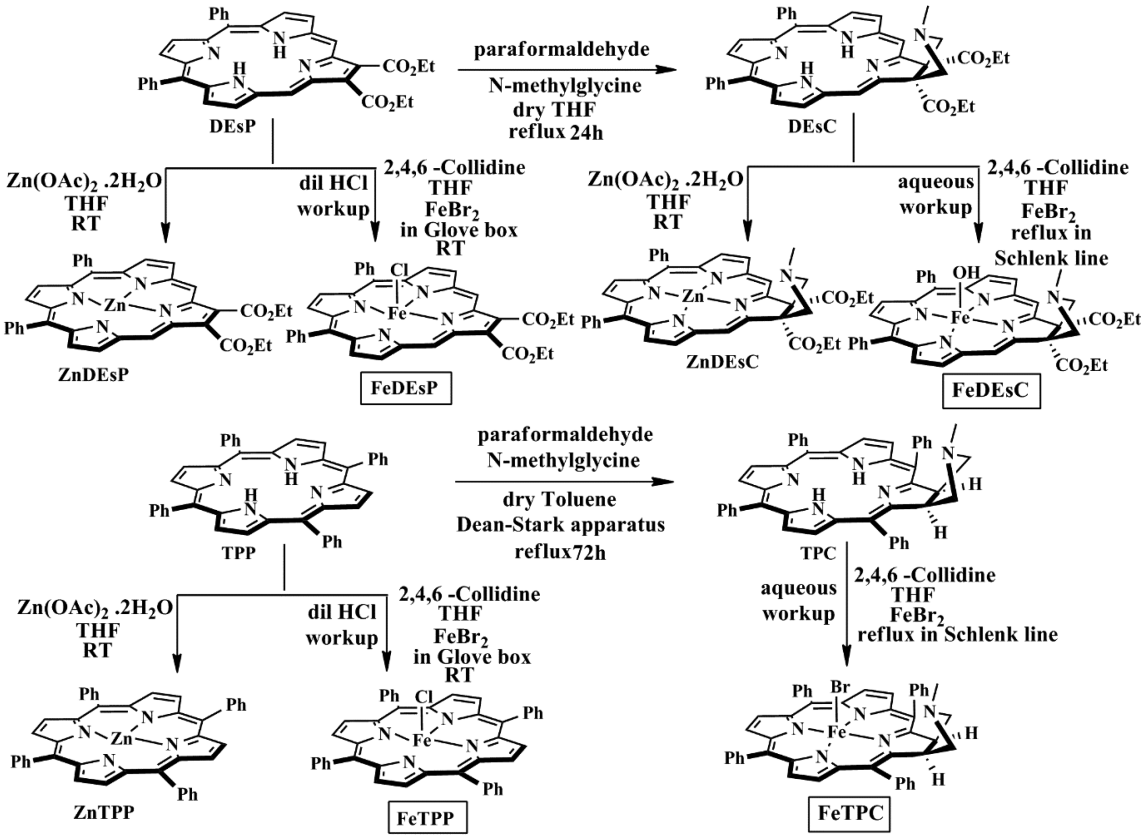

white suspension appeared because of the in situ generation of imine. A solution of DEsP (0.2 g, 0.33 mmol) in 10 mL of dry THF was added to the previous reaction mixture and refluxed for 24 h with constant monitoring by thin-layer chromatography (TLC). After a period of 5 h, the same amounts of paraformaldehyde and sarcosine were added until ∼30% conversion to the desired chlorin had taken place. THF was removed under reduced pressure. Chlorin was separated by column chromatography with silica gel (60−120 mesh size). First, DEsP was eluted with 90% DCM/hexane and chlorin with 2% MeOH/DCM as a greenish-purple oily solid, which was further purified by crashing out with pentane from a solution in MeOH. Yield: 40 ± 2% (87 ± 3 mg).

λ_{max} (DCM, nm): 418, 517, 550, 591, 658. FTIR (ν, cm^{-1}): 1704.96, 1683.74 (CO_2Et group). ^1H NMR ($CDCl_3$): δ −2.22 (s, 2H), 1.12 (t, 6H), 2.28 (s, 3H), 3.81 (d, 2H), 4.13 (d, 2H), 4.24 (q, 4H), 7.72 (s, 6H), 8.13 (m, 4H), 8.51 (s, 2H), 8.79 (d, 2H), 8.90 (d, 2H), 9.17 (s, 2H). ^{13}C NMR ($CDCl_3$, 100 MHz): δ 14.1, 61.7, 69.5, 96.5, 114.2, 119.3, 124.1, 124.2, 124.6, 126.8, 128.7, 132.5, 134.1, 135.7, 139.3, 140.5, 142.2, 147.2, 152.8, 162.1, 172.0. ESI-MS (positive-ion mode, ACN): m/z 664.1 (100%; $[M + H]^+$).

FeDEsC. To a solution of DEsC (50 mg, 0.075 mmol) in 15 mL of dry degassed THF was added 2,4,6-collidine (20 μL, 0.15 mmol) in a Schlenk flask equipped with a stopper, and the solution was stirred for 10 min in a glovebox. $FeBr_2$ (64 mg, 0.3 mmol) was added, and the flask was brought outside of the glovebox and refluxed for 3 h on the Schlenk line. After cooling to room temperature, THF was evaporated in a rotary evaporator and worked up with DCM. The organic layer was washed with a brine solution and collected. It was dried over anhydrous Na_2SO_4 and purified by column chromatography with silica gel (60−120 mesh size) using 4% MeOH/DCM mixture as the eluent. Yield: 87 ± 2% (42 ± 2 mg).

λ_{max} (DCM, nm): 406, 548, 656. ^1H NMR ($CDCl_3$): δ 83.93, 80.78, 68.09 (paramagnetic shift for β-pyrrolic ^1H's and meso ^1H's of Fe^{III}-HS complex). ESI-MS (positive-ion mode, ACN): m/z 717.3 (50%; $[M]^+$). EPR (1 mM sample in dry THF, 4 K): a rhombic signal with g values 6.25, 5.87, 5.53, and 1.97 (Figure S29).

ZnDEsC. To a solution of DEsC (50 mg, 0.075 mmol) in THF was added $Zn(OAc)_2{\cdot}2H_2O$ (82.1 mg, 0.37 mmol), and the solution was stirred for 5 h at room temperature. THF was removed under reduced pressure and purified by column chromatography with silica gel (60−120 mesh size) using a 4% MeOH/DCM mixture as the eluent. Yield: 95 ± 2% (45 ± 2 mg).

λ_{max} (DCM, nm): 410, 512, 561, 579, 604. ^1H NMR ($CDCl_3$): δ 1.13 (t, 6H), 4.25 (q, 4H), 2.00 (s, 4H), 2.35 (s, 3H), 7.68 (m, 6H), 8.04 (m, 4H), 8.30 (s, 2H), 8.57 (d, 2H), 8.69 (d, 2H), 8.78 (s, 2H). ^{13}C NMR ($CDCl_3$, 100 MHz): δ 14.1, 14.4, 20.8, 30.7, 42.0, 54.8, 61.54, 63.0, 71.1, 72.8, 97.1, 125.3, 127.5, 128.4, 129.6, 133.6, 134.8, 144.5, 147.6, 148.8, 154.7, 159.2, 173.1. ESI-MS (positive-ion mode, ACN): m/z 725.9 (15%; $[M]^+$).

TPC. Paraformaldehyde (0.1 g, 3.3 mmol) and *N*-methylglycine (0.11g, 1.32 mmol) were taken in a round-bottomed flask equipped with a Dean−Stark apparatus, attached with the Schlenk line. A total of 60 mL of dry toluene was added and refluxed for 20 min until an off-white suspension appeared, indicating in situ generation of the Schiff base. Solid TPP (0.2 g, 0.33 mmol) was added to the previous reaction mixture and refluxed for 72 h with constant monitoring by TLC. After a period of 5 h, the same amounts of paraformaldehyde and sarcosine were added until ∼50% conversion to the desired chlorin had taken place. Toluene was removed in vacuo and chlorin separated by column chromatography with silica gel (100−200 mesh size). First. the unreacted TPP was eluted with DCM and TPC with some other impurities with 1% MeOH/DCM as a greenish-purple oily residue. It was then dissolved in THF, and 50 mg of $Zn(OAc)_2{\cdot}2H_2O$ was added and stirred overnight. THF was removed in vacuo and ZnTPC separated by column chromatography with basic alumina. ZnTPC was eluted with 2% MeOH/DCM as a greenish-purple solid. Acidic workup with dilute HCl removed zinc from the cavity. The organic layer was dried over activated $MgSO_4$, filtered, and evaporated

DOI: 10.1021/acs.inorgchem.8b02063
Inorg. Chem. XXXX, XXX, XXX−XXX

to obtain a greenish-purple solid, which was immediately stored in a glovebox. Yield: 4−5% (10 ± 1 mg).

λ_{max} (DCM, nm): 419, 518, 545, 594, 647. ^{1}H NMR ($CDCl_3$): δ −1.74 (br s, 2H), 1.44 (s, 3H), 2.00 (s, 4H), 7.67−7.70 (m, 12H), 7.94 (s, 4H), 8.08−8.14 (dd, 4H), 8.25 (s, 2H), 8.44 (s, 2H), 8.59 (s, 2H). ^{13}C NMR ($CDCl_3$, 100 MHz): δ 53.0, 68.1, 112.9−152.8 (aromatic region). ESI-MS (positive-ion mode, CH_3CN): m/z 672.4 (15%; $[M + H]^+$).

FeTPC. To a solution of TPC (10 mg, 0.015 mmol) in 5 mL of dry degassed THF was added 2,4,6-collidine (5 μL, 0.03 mmol) in a Schlenk flask equipped with a stopper, and the solution was stirred for 10 min in a glovebox. $FeBr_2$ (13 mg, 0.6 mmol) was added, and the flask was brought outside the glovebox and refluxed for 3 h on the Schlenk line. After cooling to room temperature, THF was removed in vacuo and worked up with DCM. The organic layer was washed with a brine solution and collected. It was dried over anhydrous Na_2SO_4 and purified by column chromatography with silica gel (60−120 mesh size) using a 2% MeOH/DCM mixture as the eluent. After solvent evaporation, it was a purple-greenish oily residue that could not be solidified by crashing out with any binary or ternary solvent mixture with a wide range of polarities. Yield: 73 ± 1% (8 ± 0.5 mg).

λ_{max} (DCM, nm): 414, 504, 548, 599, 648. ^{1}H NMR ($CDCl_3$): δ 67.26, 75.87, 85.07 (paramagnetic shift for β-pyrrolic ^{1}H's of Fe^{III}-HS complex). ESI-MS (positive-ion mode, ACN): m/z 725.7 (100%; $[M]^+$). EPR (1 mM sample in dry THF, 77 K): an axial signal with g values of 6.02 and 1.96 (Figure S30).

Electrochemical Measurements. Four complexes (FeTPP, FeDEsP, FeTPC, and FeDEsC) were considered (Scheme 2). All cyclic voltammetry (CV) data were collected under anaerobic conditions inside a glovebox. The complexes were sparingly soluble in ACN, and sonication of the sample helped to some extent. Hence, the complexes were dissolved in 200 μL of THF, and 1800 μL of ACN was added followed by the addition of 100 mM TBAP as the supporting electrolyte. Glassy carbon was chosen as the working electrode, aqueous Ag/AgCl in saturated KCl as the reference electrode, and platinum as the counter electrode. Because the complexes had different axial ligands (Scheme 2), they were accompanied by different ligand replacement kinetics during the CV time scale. Our goal was to understand the effect of the macrocycle; thus, the CV data of the more stable, bis(imidazole) complexes were recorded. CV experiments were performed in organic solvents (THF and ACN) with ferrocene (Fc) as the internal reference, and the potential scale was normalized with respect to the potential of the Fc^+/Fc couple.

CO Complex Preparation. Dry degassed CO was generated upon the dropwise addition of deaerated concentrated H_2SO_4 to ammonium formate. The gas was passed through a 4 N KOH solution, followed by a concentrated H_2SO_4 solution. THF solution of the complexes were reduced by 0.5 equiv of a Na_2S solution (in MeOH) inside a glovebox in a properly sealed, septa-attached anaerobic vial and brought out of the box. CO gas was purged through the samples (kept in an ice bath to reduce solution evaporation) over a period of 5 min. The formation of the complexes was confirmed by UV−vis absorption and FTIR spectroscopy (data given in the Results section). The vials were perfectly sealed and used for further investigations.

NO Complex Preparation. Dry degassed NO was generated upon the dropwise addition of a deaerated saturated solution of sodium nitrite to the deaerated concentrated H_2SO_4. The gas was passed through two 4 N KOH solution bubblers, followed by one concentrated H_2SO_4 solution. The samples were prepared in the exact same way as that described in the CO Complex Preparation section using NO gas. NO complexes were also prepared in another way using Ph_3CSNO (as well as $Ph_3CS^{15}NO$), analogous to reported procedures.[47,48] To the reduced samples was added 1 equiv of Ph_3CSNO in THF. The formation of the complexes was confirmed by UV−vis absorption, FTIR, and EPR spectroscopy (data given in the Results section). The vials were perfectly sealed in septa-attached anaerobic vials and used for further investigations.

FTIR Data Collection. The samples are drop-casted onto the KBr window inside the glovebox and fitted in the anaerobic setup. The cell is brought out of the box and data collected.

UV−Vis Absorption Data Collection. All anaerobic data were collected by taking the samples from the glovebox in a tightly sealed anaerobic cuvette. The cuvette was taken out from the box, and the data were collected. The background was corrected prior to the experiments, by an identical amount of solvent mixture.

EPR Data Collection. The samples (150 μL) were taken in EPR tubes and thoroughly sealed inside the glovebox. The samples were brought from the box and frozen in liquid N_2, and the data were collected mainly at 77 K. Only for limited samples (Fe^{III}-HS) were the data collected at 4 K.

Computational Details. All calculations were performed at the IACS computer cluster using *Gaussian 03* software.[49] Both the BP86 and B3LYP functionals were tested. A mixed basis set with 6-311g* on the iron atom and on 6-31g* on the carbon, oxygen, nitrogen, and hydrogen atoms was used for optimization.[50,51] For the final energy and ground-state calculations, a 6-311+g* basis set on all atoms was used. Frequency calculations were performed using the basis set used for optimization, and no negative frequencies were found for the structures reported. The Mulliken populations were analyzed from the single-point data using *QMforge* software.[52] The relative orbital picture diagrams were drawn for the complexes, considering the orbitals with β spin. Orbital energies were normalized with respect to the d_{xy} orbital. For all complexes, a spin-unrestricted scheme was adopted, which distinguishes between α- and β-spin orbitals. The reduction potential values of the bis(imidazole) complexes and ferrocene were calculated in ACN. The solvent effect was corrected using polarizability continuum model.[53] The energy of a free electron was assumed to be −4.43 eV.[54] This was an approximation because this value will be different for different solvents. However, when the calculated $E°$ of the iron porphyrins and chlorins were referenced against $E°$ of Fc^+/Fc in the same solvent, this systematic error will cancel itself and the calculated $E°$ with respect to Fc^+/Fc can be compared to the experimental $E°$. For the CO complexes, both spin-restricted and unrestricted functionals were used; however, both produced the same frequency; hence, for all complexes, the spin-unrestricted scheme was followed. The orbital contributions were presented as a summation of the population in both the α and β orbitals of the d orbitals of iron and the 2s and 2p orbitals of the ligands. The diagram depicting the orbital overlap was drawn using *Gaussview 5.0.9* software with the isovalue of the surfaces for the corresponding molecular orbital as 0.04.

RESULTS

Synthesis. DEsP, TPP, and FeTPP were prepared following the reported procedures.[44−46] One of the pyrrole rings of the porphyrins was saturated using a 1,3-cycloaddition reaction with in situ prepared azomethine ylide. The reaction was monitored after every 5 h by TLC, and sarcosine and paraformaldehyde were added until ∼50% completion. It is worth mentioning that ∼50% conversion was the maximum obtained. Further the addition of sarcosine and paraformaldehyde led to the generation of byproducts, such as bis addition. Hence, reactions were stopped at this stage, and substrate porphyrin was recovered by column chromatography. TPC was unstable because of aerobic oxidation and, hence, was stored in a glovebox after purification. The chlorins having pendant amine groups were moisture-sensitive; hence, after synthesis of the porphyrin cores, further reactions were carried out in dry solvents. Iron porphyrins were synthesized following the usual procedures; i.e., the free-base porphyrins were deprotonated using 2,4,6-collidine and metalated with excess (∼4 equiv) $FeBr_2$ at room temperature. Metalation of the chlorins (DEsC and TPC) required refluxing of the solution. The purification procedure for the iron metalation was

DOI: 10.1021/acs.inorgchem.8b02063
Inorg. Chem. XXXX, XXX, XXX−XXX

different for porphyrins and chlorins. For porphyrins, after iron metalation, the solution was worked up with dilute HCl to remove unreacted iron salts, but this acidic workup removed iron from the chlorin cavity; thus, only an aqueous workup was done for the latter. The synthetic strategy is described in detail in Scheme 2.

X-ray Structures. *ZnDEsP.* Needle-shaped purple crystals of ZnDEsP were grown from the diffusion of hexane into a DCM solution of the complex (Figure 3). ZnDEsP crystallized

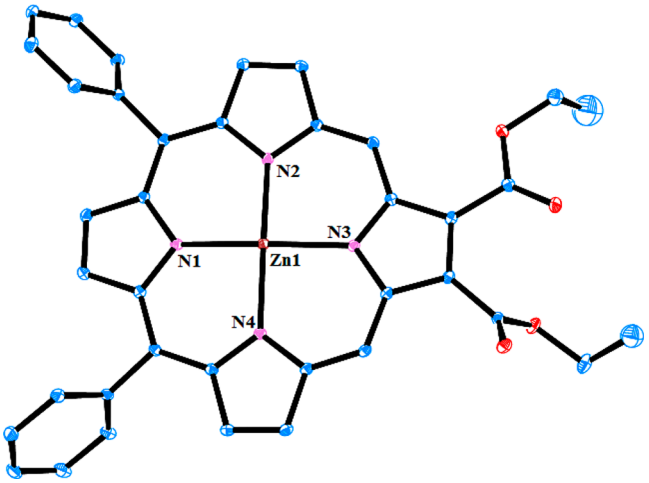

Figure 3. ORTEP diagram of the ZnDEsP complex. Color code: C, blue; Zn, brown; N, pink; O, red. Hydrogen atoms are omitted for clarity.

in a triclinic system centrosymmetric $P\bar{1}$ space group. Structural analysis revealed that it is a dimer formed by the coordination of a free carbonyl "oxygen" atom with the neighboring zinc atom (Figure S32). Zinc shows a five-coordinate distorted square-pyramidal geometry with a τ value of 0.03. The dimers are packed to form a one-dimensional chain, and the short contacts are represented in Figure S35.

FeDEsP. Greenish-purple needlelike crystals of FeDEsP were grown from the slow evaporation of a THF solution. SCXRD analysis revealed that it is a μ-oxo dimer ((Figure 4) and crystallized in a monoclinic system with a centrosymmetric $P2_1/c$ space group. Both iron atoms show five-coordinate

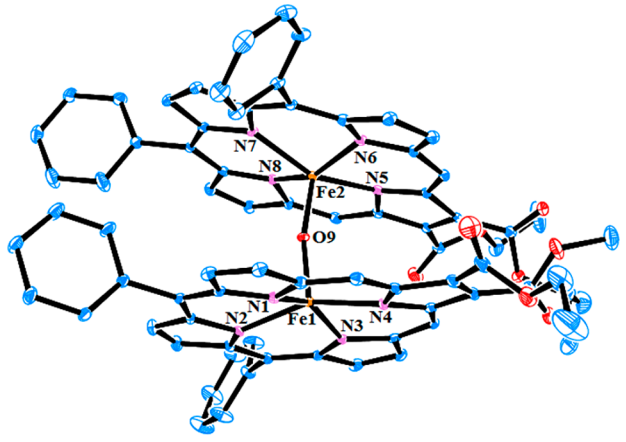

Figure 4. ORTEP diagram of the $(FeDEsP)_2O$ complex. Color code: C, black; Fe, brown; N, blue; O, red. Hydrogen atoms are omitted for clarity.

distorted square-pyramidal geometry with a τ value of 0.04. The dimers are likely packed through C−H···O hydrogen-bonding interactions to form a three-dimensional supramolecular structure (Figure S36). All of the hydrogen-bonding dimensions are summarized in Table S1. The molecular structure is given in Figure S33.

ZnDEsC. Purple platelike crystals were grown through the slow diffusion of diethyl ether to the chloroform solution of ZnDEsC. It crystallized in an orthorhombic *Pnma* space group (Figure 5). Zinc shows a five-coordinate distorted square-

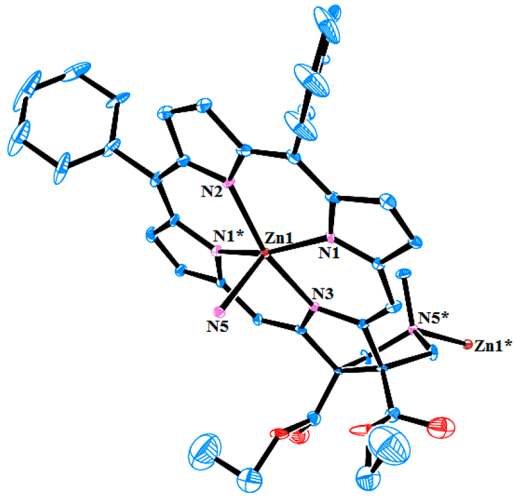

Figure 5. ORTEP diagram of the ZnDEsC complex. Color code: C, gray; Zn, pink; N, blue; O, red. Hydrogen atoms and solvent molecules are omitted for clarity.

pyramidal geometry with a τ value of 0.03. During crystal packing, the nitrogen center of the azomethine unit of each ZnDEsC moiety interacted with the zinc(II) center, making a one-dimensional coordination polymeric chain (Figure S34).

CV. The iron-bound porphyrinoids showed quasi-reversible iron(III/II) processes (Figure 6). The iron(III/II) reduction potential of $FeDEsP(Im)_2$ was ∼160 mV more positive than that of $FeTPP(Im)_2$. This suggests that replacing two β-pyrrolic hydrogen atoms from the porphyrin ring with two

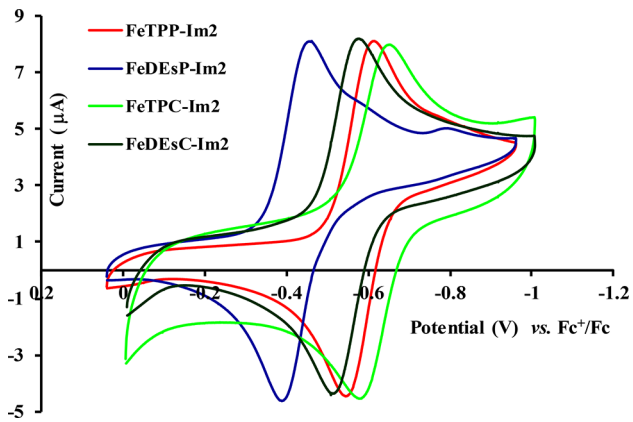

Figure 6. Cyclic voltammograms of the complexes in THF/ACN (1:9) at room temperature. The working electrode was glassy carbon, the counter electrode was platinum, and the reference electrode was aqueous Ag/AgCl in saturated KCl. TBAP wa used as the supporting electrolyte (100 mM).

DOI: 10.1021/acs.inorgchem.8b02063
Inorg. Chem. XXXX, XXX, XXX−XXX

electron-withdrawing ester groups shifted the reduction potential positive. On the contrary, upon saturation of one of the pyrrole rings of FeTPP, the iron(III/II) reduction potential was lowered by ~30 mV in FeTPC$(Im)_2$. FeDEsC-$(Im)_2$ contains both electron-withdrawing groups and a saturated pyrrole center. The iron(III/II) reduction potential of FeDEsC$(Im)_2$ was ~120 mV more negative with respect to FeDEsP$(Im)_2$. Thus, insertion of the electron-withdrawing groups at the β-pyrrolic positions of porphyrin shifted the iron(III/II) potential to a positive value, while saturation of the same positions shifted the potential to a negative value.

CO Complexes. CO adduct formation was characterized by UV−vis absorption and IR spectroscopy.

UV−Vis Absorption. Upon the addition of CO gas to the reduced porphyrins (i.e., Fe^{II}TPP and Fe^{II}DEsP), the color of the solution changed from pinkish red to dark red, while for the same treatment for the chlorins (i.e., Fe^{II}TPC and Fe^{II}DEsC), the light-green solution changed to intense green (Figure S37). Upon CO addition to Fe^{II}TPP, a blue shift in the Soret band occurred from 434 to 417 nm. In the Q-band region, the 617 nm peak diminished and the 580 nm peak intensified. In the case of Fe^{II}DEsP-CO, the Soret band shifted from 431 to 418 nm, and in the Q-band region, the 613 nm peak intensified at the expense of the intensities of the 536 and 573 nm peaks. For Fe^{II}TPC-CO, the Soret band shifted from 422 to 414 nm, and in the Q-band region, the intense peak at 606 nm shifted to 649 nm. In the case of Fe^{II}DEsC-CO, a small change in the Soret band (from 414 to 413 nm) was accompanied by the disappearance of the 540 and 637 nm peaks and a new peak at 594 nm appeared in the Q-band region.

FTIR. The addition of CO gas in the solution of iron(II) samples was accompanied by the rise of a very intense band corresponding to the ν_{C-O} stretch in the range of 1960−1980 cm^{-1} (Figure 7). The C−O stretching vibrations (ν_{C-O}) appeared at 1966, 1975, 1978, and 1973 cm^{-1} for the complexes Fe^{II}TPP-CO, Fe^{II}DEsP-CO, Fe^{II}TPC-CO, and Fe^{II}DEsC-CO, respectively.

NO Complexes. NO adduct formation was characterized UV−vis absorption, IR, and EPR spectroscopy.

UV−Vis Absorption. NO adduct formations were accompanied by the color change akin to the CO adduct formation (Figure S38). Upon the addition of NO gas to Fe^{II}TPP, there was a blue shift in the Soret band from 434 to 414 nm. In the Q-band region, the 579 and 617 nm peaks disappeared and a new peak was generated at 540 nm. For the Fe^{II}DEsP-NO complex, the Soret band shifted from 431 to 417 nm, and in the Q-band region, two new peaks were generated at 554 and 580 nm at the expense of the 536, 613, and 573 nm peaks. In the case of the Fe^{II}TPC-NO complex, it was accompanied by a sharp change in the Soret band from 422 to 413 nm, and in the Q-band region, the 606 nm intense peak shifted to 617 nm. For the Fe^{II}DEsC complex, NO addition led to a small change in the Soret band from 414 to 405 nm, and in the Q-band region, the 594 nm peak shifted to 602 nm.

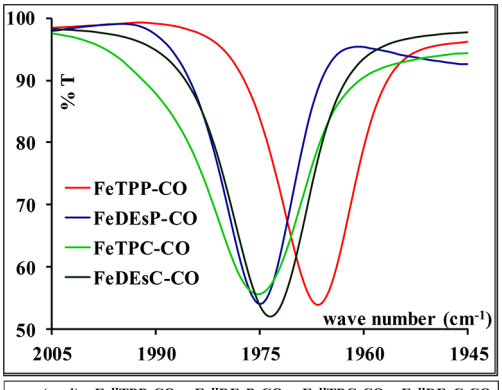

ν_{C-O} (cm^{-1})	Fe^{II}TPP-CO	Fe^{II}DEsP-CO	Fe^{II}TPC-CO	Fe^{II}DEsC-CO
Expt.	1966	1975	1978	1973

Figure 7. FTIR data of the CO complexes drop-casted onto a KBr window. The experimental values are tabulated below.

FTIR. The addition of NO to the solution of iron(II) samples resulted in the rise of a very intense band corresponding to N−O stretching vibration (ν_{N-O}) in the range of 1660−1690 cm^{-1} (Figure 8). For the Fe^{II}TPP-^{14}NO complex, the $\nu^{14}{}_{N-O}$ vibration appeared at 1674 cm^{-1}, and upon ^{15}N substitution (^{15}NO), the N−O vibration band shifted to 1645 cm^{-1}. Similarly, for the Fe^{II}DEsP-NO complex, the $\nu^{14}{}_{N-O}$ vibration appeared at 1683 cm^{-1} and the corresponding ^{15}N−O vibration band shifted to 1647 cm^{-1}. For the Fe^{II}TPC-NO complex, the ^{14}N−O vibration band appeared at 1627 cm^{-1}, and it shifted to 1598 cm^{-1} upon ^{15}N substitution. For the Fe^{II}DEsC-NO complex, the $\nu^{14}{}_{N-O}$ vibration appeared at 1688 cm^{-1}, and it shifted to 1651 cm^{-1} upon ^{15}N substitution. Therefore, the N−O stretches (ν_{N-O}) for the Fe^{II}TPP-NO, Fe^{II}DEsP-NO, and Fe^{II}DEsC-NO complexes were in the range typical for 5C ferrous heme NO complexes, while ν_{N-O} for the Fe^{II}TPC-NO complex was in the range typical for 6C ferrous heme NO complexes. So, it is likely to be a MeOH-bound six-coordinate Fe^{II}-TPC(NO)-(MeOH) complex.

EPR. The parent iron(II) complexes were EPR-silent in perpendicular-mode X-band EPR. Ferrous heme nitrosyls of the general formula $\{Fe(heme)(NO)\}^7$ in proteins and model complexes exhibited low-spin ground states of $S = {}^1/_2$ total spin. 5C ferrous heme nitrosyls exhibited characteristic EPR spectra with average g values of about 2.10, 2.06 and 2.01, while the g values for 6C complexes were about 2.08, 2.00, and 1.98 and, hence, were markedly smaller than those for their 5C analogues. The three-line hyperfine pattern originated from the nuclear spin $I = 1$ of ^{14}N, and the corresponding two-line hyperfine pattern originated from the nuclear spin $I = {}^1/_2$ of ^{15}N. The experimental data are shown in Figure 9. Both the experimental and simulated (Figure S40) g and A values were in good agreement with each other (Tables S3 and S4). The data suggested that these complexes form a six-coordinate NO adduct at low temperature (77 K). This attributed to the lower entropic contribution at low temperature, forming a 6C $\{FeNO\}^7$ complex binding a solvent molecule (MeOH).[55]

Density Functional Theory (DFT) Calculations. The experimentally found iron(III/II) reduction potential values suggested that the addition of electron-withdrawing groups shifted the reduction potentials to positive value, while upon saturation of one of the pyrroles of the porphyrin, the reduction potential shifted to a negative value. The ν_{C-O} and ν_{N-O} values obtained from FTIR experiments of the CO and NO complexes, respectively, showed that, upon the addition of electron-withdrawing groups or upon saturation of one of the pyrrole rings, the C−O and N−O stretching frequencies increased relative to the reference FeTPP complex. This implies that perturbation on the structure of porphyrin affected the electronic structure of the corresponding iron complexes. Hence, DFT calculations were used to gain insight into it. The

DOI: 10.1021/acs.inorgchem.8b02063
Inorg. Chem. XXXX, XXX, XXX−XXX

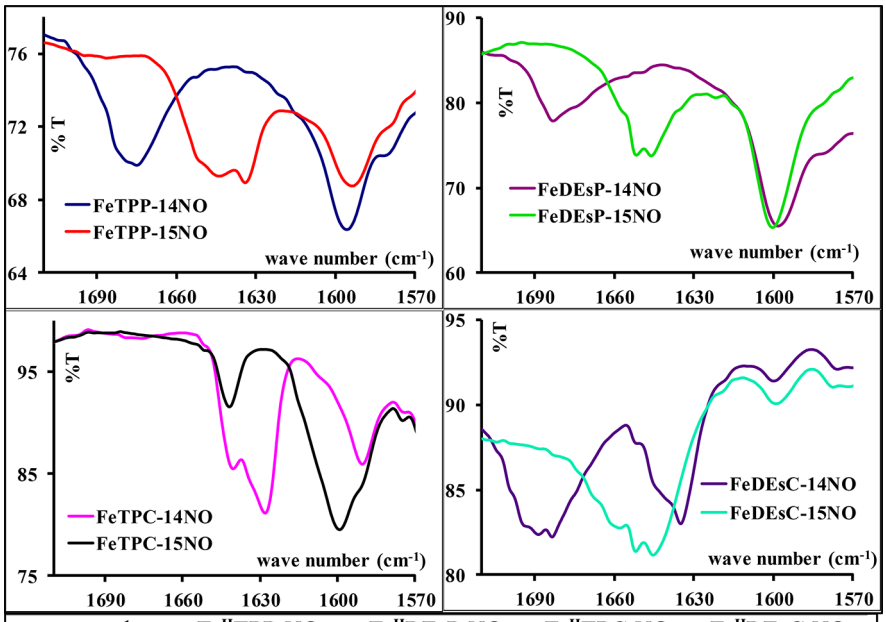

ν_{N-O} (cm^{-1})	Fe^{II}TPP-NO (^{15}NO)	Fe^{II}DEsP-NO (^{15}NO)	Fe^{II}TPC-NO (^{15}NO)	Fe^{II}DEsC-NO (^{15}NO)
Expt.	1674 (1645)	1683 (1647)	1627 (1598)	1688 (1651)

Figure 8. FTIR data of the NO complexes drop-casted onto a KBr window. The experimental values are tabulated below.

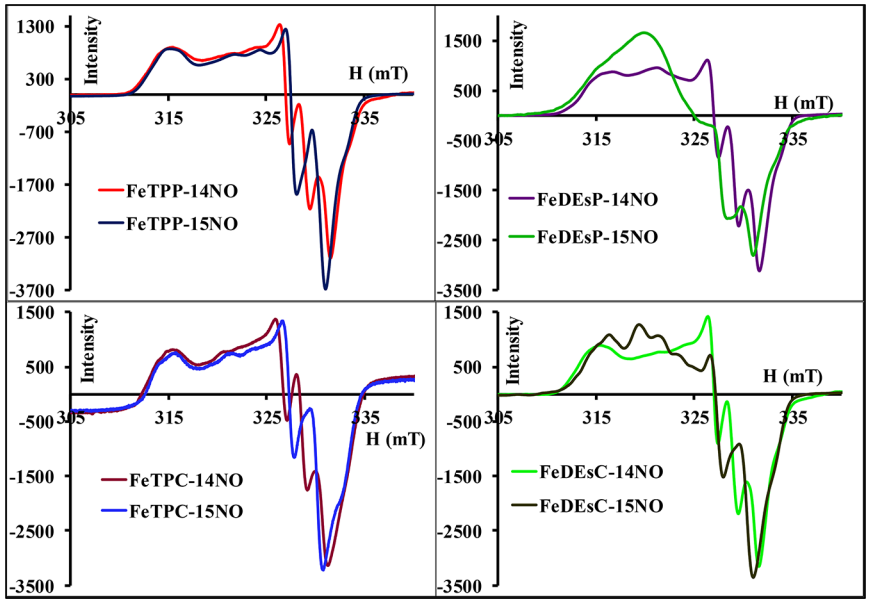

Figure 9. EPR spectra of ^{14}NO- and ^{15}NO-bound complexes, respectively (MW frequency, 9135.3 MHz; center field, 320 mT; MW power, 1 mW; modulation frequency, 0.25 mT).

DFT-optimized structures were compared with the crystal structures. The average metal pyrrole bond lengths from the experiments closely matched with the calculated values (Table 1).

CO Complexes. The Fe^{II}-CO complexes were optimized using the BP86 and B3LYP functionals. The calculated C−O stretching frequencies are given in Table 2.

The frequencies obtained from the BP86 functional are in better agreement with the experimental values (Figure 7).

Table 1. Metal−Ligand Bond Lengths Obtained from the Crystal Structures and DFT-Optimized Structures

ave M−N_{pyr} bond length (Å)	crystal structure	DFT-optimized
ZnDEsP	2.049	2.046
FeDEsP	2.072	2.094
ZnDEsC	2.085	2.058

NO Complexes. The Fe^{II}-NO complexes were optimized using the BP86 and B3LYP functionals. The calculated C−O stretching frequencies are given in Table 3.

DOI: 10.1021/acs.inorgchem.8b02063
Inorg. Chem. XXXX, XXX, XXX−XXX

Table 2. DFT-Calculated C−O Stretching Frequencies

	ν_{C-O} (cm^{-1})			
	Fe^{II}TPP-CO	Fe^{II}DEsP-CO	Fe^{II}TPC-CO	Fe^{II}DEsC-CO
expt	1966	1975	1978	1973
uBP86	1980	1985	1981	1983
uB3LYP	2090	2097	2094	2096

Table 3. DFT-Calculated N−O Stretching Frequencies

	ν_{N-O} (cm^{-1})			
	Fe^{II}TPP-NO (5C)	Fe^{II}DEsP-NO (5C)	Fe^{II}TPC-NO (6C)	Fe^{II}DEsC-NO (5C)
expt	1674	1683	1627	1688
uBP86	1707	1726	1704	1713
uB3LYP	1768	1810	1820	1782

The calculated ν_{C-O} and ν_{N-O} frequencies obtained from the BP86 functional were in better agreement with the experimental values (Figures 7 and 8); hence, further analysis was carried out with the BP86 functional.

Iron(III/II) Reduction Potential. The reduction potential values of the bis(imidazole) complexes and ferrocene were calculated using the BP86 functional (Table 4). The calculated $E°$ iron(III/II) reduction potential of the iron porphyrins and chlorins were referenced against the calculated $E°$ iron(III/II) of Fc^+/Fc. In ACN, the iron(III/II) reduction potential of FeTPP-Im_2 was found to be −0.71 V, while for FeDEsP-Im_2, it was −0.52 V. However, in FeDEsP, two *meso*-phenyl groups were substituted by hydrogen. Hence, iron diphenylporphyrin, FeDPP$(Im)_2$, was considered for a comparison by DFT. The calculated redox potential was −0.70 V, which closely resembled the value obtained from FeTPP-Im_2; hence, the difference in the redox potential between FeTPP and FeDEsP was solely due to the electron-withdrawing groups. For FeTPC-Im_2, the potential was −0.87 V, which was negatively shifted from that of FeTPP-Im_2. For FeDEsC-Im_2, the potential was found to be at −0.78 V, which was shifted to lower values relative to that of FeDEsP-Im_2. Therefore, the trend obtained from the calculated $E°$ values was in good agreement with that from the experimental $E°$ values.

DISCUSSION

The addition of electron-withdrawing groups and/or saturation of one of the pyrrole rings of the porphyrin resulted in changes in the electronic structures of porphyrins, which is reflected in the iron(III/II) reduction potential as well as in their corresponding CO and NO vibrations of the adducts. DFT calculations reasonably reproduced the trends in the experimental data and were used to further analyze the ground-state wave functions. The effects of the electron-withdrawing group and saturation are discussed separately, and finally the combined effect is discussed.

Effect of the Electron-Withdrawing Group. The iron(III/II) reduction potential of FeDEsP-Im_2 was more positive than that of FeTPP-Im_2 (Table 4). The iron(III/II) reduction potential depended on two factors: (a) the electron affinity of the iron(II) center and/or (b) the stability of iron(II). The electron affinity of iron(III) was judged from the natural population analysis (NPA) and natural bond orbital (NBO) analysis, which gave the natural charge over the atoms.[56] Both analyses suggested that the natural charge over iron was slightly higher in the case of Fe^{III}DEsP-Im_2 relative to Fe^{III}TPP-Im_2 (Table 5). The inductive withdrawing (−I) effect of the ester groups was responsible for making the iron center in Fe^{III}DEsP-Im_2 more electropositive than that of Fe^{III}TPP-Im_2. As a result, Fe^{III}DEsP-Im_2 had greater electron affinity over Fe^{III}TPP-Im_2.

Table 5. Theoretically Calculated Natural Charge over Iron in the Corresponding Bis(imidazole) Complexes Using the uBP86 Functional in Both the NPA and NBO Methods

	natural charge over iron	
	NPA	NBO
FeTPP-Im_2	0.49	0.19
FeDEsP-Im_2	0.52	0.21
FeTPC-Im_2	0.49	0.19
FeDEsC-Im_2	0.50	0.20

The electron-withdrawing ester groups exerted the −I effect, making the ligand (pyrrolic nitrogen atoms of the porphyrin) a weak σ donor. This should result in a relatively weaker interaction between the porphyrin and $d_{x^2-y^2}$ orbital of iron. The relative molecular orbital diagram of the corresponding bis(imidazole) complexes (to minimize the axial ligand effect) did not show any significant change in the energy of the $d_{x^2-y^2}$ orbital (Figure S41). This implies that the ester groups may not have a prominent effect in σ bonding; they should be involved mainly in π interaction. In fact, the Mulliken population analysis[56] of reduced Fe^{II}DEsP-Im_2 indicates that there was greater mixing between the iron(II) and π^* orbitals of the DEsP macrocycle (DEsP−π^*), relative to TPP−π^* (of Fe^{II}TPP-Im_2), which was responsible for greater charge delocalization in the reduced [iron(II)] porphyrin, making FeDEsP-Im_2 easy to be reduced compared to FeTPP-Im_2 (Figure 10 and Table 6).

The ν_{C-O} value for Fe^{II}TPP-CO was at 1966 cm^{-1}, which increased to 1975 cm^{-1} for Fe^{II}DEsP-CO. The corresponding NO complexes showed similar trends. The ν_{N-O} value for Fe^{II}TPP-NO was at 1974 cm^{-1}, which increased to 1983 cm^{-1} for Fe^{II}DEsP-NO. Both indicated a lowering in back-bonding from Fe d_{xz}/d_{yz} to the π^* orbitals of CO/NO. The Mulliken population analysis suggested that in FeDEsP less mixing occurred between Fe d_{xz}/d_{yz} and the π^* orbitals of CO/NO relative to the corresponding CO/NO complexes of FeTPP (Tables 7 and 8). On the contrary, the mixing between Fe d_{xz}/d_{yz} and the porphyrin−π^* orbitals increased in both CO/NO complexes of FeDEsP compared to Fe^{II}TPP-CO/NO. Previously, Ryan et al. had reported the reduction of N−O

Table 4. Experimentally and Theoretically Calculated Reduction Potential Values of the Bis(imidazole) Complexes

	$E°(Fe^{III/II})$ vs Fc^+/Fc (V)				
	FeTPP$(Im)_2$	FeDEsP$(Im)_2$	FeDPP$(Im)_2$	FeTPC$(Im)_2$	FeDEsC$(Im)_2$
experimental	−0.58	−0.42		−0.61	−0.54
theoretical	−0.71	−0.52	−0.70	−0.87	−0.78

DOI: 10.1021/acs.inorgchem.8b02063
Inorg. Chem. XXXX, XXX, XXX−XXX

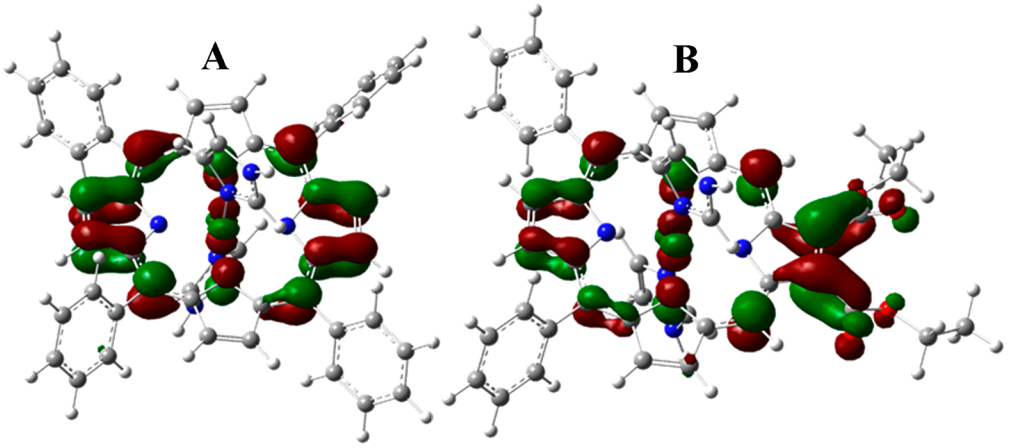

Figure 10. Orbital overlap between the iron and π^* orbitals of the porphyrin macrocycle for the (A) $Fe^{II}TPP\text{-}Im_2$ and (B) $Fe^{II}DEsP\text{-}Im_2$ complexes.

Table 6. Summation of Mulliken Population of the Iron(II) Orbitals (d_{xz} and d_{yz}) in the π^* Orbitals ($\alpha + \beta$) of the Porphyrin Macrocycle

iron orbital content	[P−π^*]	iron orbital content	[P−π^*]
$Fe^{II}TPP\text{-}Im_2$	33.02	$Fe^{II}TPC\text{-}Im_2$	30.78
$Fe^{II}DEsP\text{-}Im_2$	34.24	$Fe^{II}DEsC\text{-}Im_2$	30.36

Table 7. Orbital Contributions of the Respective d Orbitals ($\alpha + \beta$) of Iron in Macrocycle−π^* and CO−π^* Orbitals

	contribution of iron		
	CO−$\pi_1^*{}_{ab}$	CO−$\pi_2^*{}_{ab}$	[P−π^*]
$Fe^{II}TPP\text{-}CO$	26.58	27.58	11.36
$Fe^{II}DEsP\text{-}CO$	24.48	24.80	11.62
$Fe^{II}TPC{-}CO$	22.00	25.68	12.32
$Fe^{II}DEsC{-}CO$	27.64	24.28	11.04

Table 8. Orbital Contributions of the Respective d Orbitals ($\alpha + \beta$) of Iron in NO−π^* and Macrocycle−π^* Orbitals

	contribution of iron	
	NO−π_v^*	[P−π^*]
$Fe^{II}TPP\text{-}NO$	67.81	19.68
$Fe^{II}DEsP\text{-}NO$	53.95	27.61
$Fe^{II}TPC\text{-}NO$	44.96	23.23
$Fe^{II}DEsC\text{-}NO$	46.59	24.45

stretching frequency in $[FeNO]^7$ species with octaethylporphyrin because the pyrrole rings were oxidized to pyrrolidones in contrast to observations here, suggesting a different effect of pyrrole oxidation on back-bonding from iron to NO.[32]

Therefore, a competitive back-bonding between macrocycle−π^* and the axial ligand π^* with the Fe d_{xz}/d_{yz} orbitals was operative here (Scheme 3). The extent of back-bonding was responsible for tuning of the reduction potential and its reactivity. Hence, iron porphyrins with electron-withdrawing groups attached with the β-pyrroles exerted a relatively positive reduction potential and made the CO and NO adducts weaker. The effect that arose from the presence of the electron-withdrawing groups can be extended to O_2 reactivity. The O_2 binding site in CcO is heme a_3, while the O_2 carrier protein hemoglobin/myoglobin contain heme b. The difference between heme a_3 and heme b was that in heme a_3 the C_3

Scheme 3. Effect of Back-Bonding in the X−O (X = C, N) Stretching Frequency: Competitive Back-Bonding between Macrocycle−π^* and Axial Ligand π^*

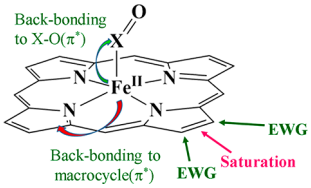

and C_{18} positions of heme b were replaced by two electron-withdrawing groups: hydroxyfarnesyl and a formyl group, respectively (Figure 1A).[9] Because of the electron-withdrawing groups attached with the β-pyrroles of the heme increased the iron(III/II) reduction potential, it can reduce O_2 to water at a very low overpotential.[44] In fact, the iron(III/II) potential of CcO is ∼350 mV, which is much higher than that of Hb/Mb (−200 mV). A significant part of this difference may be derived from the -I effect of the formyl and hydroxyfarnesyl groups.[23] A weakly bound CO or NO adduct may be an alternative defense mechanism against the inhibitions by them.

Effect of Saturation of One of the Pyrrole Rings. The reduction potential of $FeTPC\text{-}Im_2$ was negative relative to $FeTPP\text{-}Im_2$ (Table 4). The relative energy level diagram suggested that, upon saturation of one of the pyrrole rings of the porphyrin, the energy of the d_{z^2} orbital decreased by 0.26 eV and that of the $d_{x^2-y^2}$ orbital increased by 0.15 eV (Figure S42). Weaker interaction with the axial imidazole lowered the energy of the d_{z^2} orbital. The $d_{x^2-y^2}$ orbital became more destabilized because of the stronger σ donation from of the pyrrolic nitrogen atoms. Hence, saturation exerted a +I effect to make the pyrrole nitrogen atom a better σ donor. The Mulliken population analysis indicated a relatively lower mixing between the iron(II) and π^* orbitals of the chlorin macrocycle (TPC−π^*), in comparison with porphyrin (TPP−π^*; Table 6). In $Fe^{II}TPC\text{-}Im_2$, back-bonding with the macrocycle−π^* orbitals was weaker because the planarity of the TPC macrocycle was compromised because of the weak hydrogen-bonding interaction between the pendant amine and axial imidazole (Figure S31). Therefore, in $Fe^{II}TPC\text{-}Im_2$, less charge delocalization from iron(II) to the macrocycle π^* orbital occurred relative to $Fe^{II}TPP\text{-}Im_2$, and hence the former was relatively difficult to reduce, which was reflected in the

DOI: 10.1021/acs.inorgchem.8b02063
Inorg. Chem. XXXX, XXX, XXX−XXX

Scheme 4. Plausible Mechanistic Pathway of Nitrite Reduction Catalyzed by CcNiR and Cd_1NiR

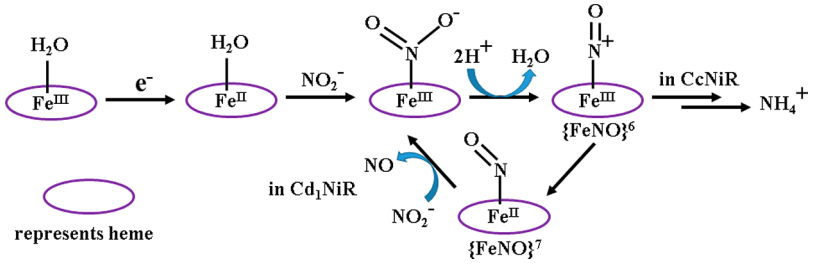

reduction potential values. The ν_{C-O} value for five-coordinate Fe^{II}TPP-CO was at 1966 cm^{-1}, which shifted to 1978 cm^{-1} for Fe^{II}TPC-CO (Figure 7), which was due to less back-bonding to the π^* orbitals of CO because of competitive back-bonding (Table 7).

The Fe^{II}TPC formed a six-coordinate $\{FeNO\}^7$ complex at room temperature where the sixth ligand was likely the solvent MeOH. Lehnert et al. showed that the NO in $\{FeNO\}^7$ complexes has a much stronger trans effect than that in the corresponding $\{FeNO\}^6$ complexes because of the much stronger σ bonding in the former.[57,58] Fe^{II}TPC formed a six-coordinate Fe^{II}TPC(NO)(*N*-methylimidazole) complex with only 1 equiv of *N*-methylimidazole, while in the case of Fe^{II}TPP, excess *N*-methylimidazole was required to form the six-coordinate Fe^{II}TPP(NO)(*N*-methylimidazole) complex. The N−O stretching vibration appeared at 1627 cm^{-1}, which shifted to 1598 cm^{-1} upon ^{15}N substitution (Figure S19). The N−O stretching vibrations clearly indicated that back-bonding to NO−π^* was significantly low in Fe^{II}TPC(NO)(*N*-methylimidazole), relative to its FeTPP analogue. While the strength of the σ bond drove the trans effect, as pointed out by Lehnert et al., the Mulliken population analysis indicated that back-bonding from Fe^{II} dπ to NO π^* was lower as well in Fe^{II}TPC(NO), likely because of the synergistic effect, relative to Fe^{II}TPP(NO) (Table 8), which was reflected in their relative NO frequencies; i.e., the NO vibration acted as a spectator to the dominantly σ-bonding effect. Therefore, saturating the 3 and 4 positions of one of the pyrrole rings of the porphyrin weakened both σ bonds and exerted lower back-bonding to the axial ligand (CO and NO) relative to the fully unsaturated FeTPP.

FeDEsC is a system in which both the electron-withdrawing group and saturated pyrrole center is present together. These two substitutions have opposite effects on the redox potential: the electron-withdrawing group makes it positive, while saturation reduces it. As a result, FeDEsC-Im_2 showed a redox potential that was higher than that of FeTPP-Im_2 (because of its electron-withdrawing effects) but lower than FeDEsP-Im_2 (because of the saturation). It was observed that both the electron-withdrawing and saturation effects led to lower back-bonding to the CO/NO π^* orbitals. Therefore, the higher C−O and N−O stretching frequencies of Fe^{II}DEsC-CO and Fe^{II}DEsC-NO, respectively, stemmed from a consequence of competitive back-bonding (Scheme 3).

FeDEsC can be structurally correlated with heme d_1 in Cd_1NiR, which contains two electron-withdrawing formyl groups and two saturated pyrrole carbon atoms (Figure 1C).[11] Cd_1NiR, a nitrite reducing enzyme, terminates the reduction cycle at NO, in strict contrast to CcNiR, a multi-c-heme-containing enzyme, which reduces nitrite to an ammonium ion without releasing NO (Figure 1B).[10] Both nitrite-reducing enzymes follow similar mechanistic pathways until the formation of a $\{Fe(NO)\}^6$ intermediate (Scheme 4). However, in the case of Cd_1NiR, it takes one electron from cytochrome *c* and NO is released, while in CcNiR, the reaction cycle continues until the formation of an ammonium ion. The fast NO dissociation ($k_{off} \sim 6-35$ s^{-1}) from ferrous cd_1 nitrite reductase supports the argument.[59] Iron porphyrin possessing both electron-withdrawing groups and a saturated center forms weakly bound NO adduct $\{FeDEsC\text{-}NO\}^7$ relative to the situation where iron porphyrin is having only electron-withdrawing groups, $\{FeDEsP\text{-}NO\}^7$. Hence, in the $\{FeNO\}^7$ intermediate of heme d_1 in Cd_1NiR, the NO adduct should be so weakly bound (due to competitive back-bonding) that NO can be released prior to a further reduction to ammonium.

CONCLUSIONS

In this Article, we have discussed how perturbation of iron porphyrinoids can alter the electronic structure, by introducing electron-withdrawing groups to the β-pyrrolic positions and by saturating the same. The electron-withdrawing group (−I effect) and saturation (+I effect) have little effect on the σ bonding between macrocycles and the iron. Instead, they affect the π bonding by lowering the energy of the π^* orbitals of the porphyrin ring. Therefore, resulting in a competitive back-bonding scenario between Fe dπ and (a) the NO/CO π^* and (b) the vacant porphyrin−π^* orbitals. Electron-withdrawing groups significantly increase the iron(III/II) reduction potential, which is also relevant to heme a_3 in CcO. The electron-withdrawing group and saturation together form a very weakly bound ferrous nitrosyl complex, which is hypothesized as the reason why heme d_1 in Cd_1NiR releases NO from the $\{FeNO\}^7$ intermediate.

ASSOCIATED CONTENT

Supporting Information

The Supporting Information is available free of charge on the ACS Publications website at DOI: 10.1021/acs.inorgchem.8b02063.

Additional NMR, mass, UV−vis, and FTIR data and coordination of the DFT-optimized structures (PDF)

Accession Codes

CCDC 1854375−1854377 contain the supplementary crystallographic data for this paper. These data can be obtained free of charge via www.ccdc.cam.ac.uk/data_request/cif, or by emailing data_request@ccdc.cam.ac.uk, or by contacting The Cambridge Crystallographic Data Centre, 12 Union Road, Cambridge CB2 1EZ, UK; fax: +44 1223 336033.

DOI: 10.1021/acs.inorgchem.8b02063
Inorg. Chem. XXXX, XXX, XXX−XXX

AUTHOR INFORMATION

Corresponding Author

*E-mail: icad@iacs.res.in.

ORCID

Abhishek Dey: 0000-0002-9166-3349

Notes

The authors declare no competing financial interest.

ACKNOWLEDGMENTS

This research is funded by Council of Scientific and Industrial Research (CSIR) Grant 01(2874)/17/EMR-II. S.A. acknowledges CSIR-SRF, and P.S. acknowledges UGC-JRF.

REFERENCES

(1) Munro, A. W.; Girvan, H. M.; McLean, K. J.; Cheesman, M. R.; Leys, D. Heme and Hemoproteins. In *Tetrapyrroles: Birth, Life and Death*, Warren, M. J., Smith, A. G., Eds.; Springer: New York, 2009; pp 160−183.

(2) Heinemann, I. U.; Jahn, M.; Jahn, D. The biochemistry of heme biosynthesis. *Arch. Biochem. Biophys.* **2008**, *474* (2), 238−251.

(3) Battersby, A. R.; McDonald, E. Origin of the pigments of life: the type-III problem in porphyrin biosynthesis. *Acc. Chem. Res.* **1979**, *12* (1), 14−22.

(4) Cornah, J. E.; Terry, M. J.; Smith, A. G. Green or red: what stops the traffic in the tetrapyrrole pathway? *Trends Plant Sci.* **2003**, *8* (5), 224−230.

(5) Raux-Deery, E.; Leech, H. K.; Nakrieko, K.-A.; McLean, K. J.; Munro, A. W.; Heathcote, P.; Rigby, S. E. J.; Smith, A. G.; Warren, M. J. Identification and Characterization of the Terminal Enzyme of Siroheme Biosynthesis from Arabidopsis thaliana: A PLASTID-LOCATED SIROHYDROCHLORIN FERROCHELATASE CONTAINING A 2FE-2S CENTER. *J. Biol. Chem.* **2005**, *280* (6), 4713−4721.

(6) Warren, M. J.; Scott, A. I. Tetrapyrrole assembly and modification into the ligands of biologically functional cofactors. *Trends Biochem. Sci.* **1990**, *15* (12), 486−491.

(7) Warren, M. J.; Stolowich, N. J.; Santander, P. J.; Roessner, C. A.; Sowa, B. A.; Scott, A. I. Enzymatic synthesis of dihydrosirohydrochlorin (precorrin-2) and of a novel pyrrocorphin by uroporphyrinogen III methylase. *FEBS Lett.* **1990**, *261* (1), 76−80.

(8) Schön, A.; Krupp, G.; Gough, S.; Berry-Lowe, S.; Kannangara, C. G.; Söll, D. The RNA required in the first step of chlorophyll biosynthesis is a chloroplast glutamate tRNA. *Nature* **1986**, *322*, 281.

(9) Yoshikawa, S.; Shinzawa-Itoh, K.; Nakashima, R.; Yaono, R.; Yamashita, E.; Inoue, N.; Yao, M.; Fei, M. J.; Libeu, C. P.; Mizushima, T.; Yamaguchi, H.; Tomizaki, T.; Tsukihara, T. Redox-Coupled Crystal Structural Changes in Bovine Heart Cytochrome c Oxidase. *Science* **1998**, *280* (5370), 1723.

(10) Einsle, O.; Messerschmidt, A.; Huber, R.; Kroneck, P. M. H.; Neese, F. Mechanism of the Six-Electron Reduction of Nitrite to Ammonia by Cytochrome c Nitrite Reductase. *J. Am. Chem. Soc.* **2002**, *124* (39), 11737−11745.

(11) Nurizzo, D.; Silvestrini, M. C.; Mathieu, M.; Cutruzzola, F.; Bourgeois, D.; Fulop, V.; Hajdu, J.; Brunori, M.; Tegoni, M.; Cambillau, C. N-terminal arm exchange is observed in the 2.15 A crystal structure of oxidized nitrite reductase from Pseudomonas aeruginosa. *Structure (Oxford, U. K.)* **1997**, *5* (9), 1157−71.

(12) Begley, T.; Ortiz de Montellano, P. R. Hemes in Biology. *Wiley Encyclopedia of Chemical Biology*; Wiley: New York, 2008.

(13) Poulos, T. L. Heme Enzyme Structure and Function. *Chem. Rev.* **2014**, *114* (7), 3919−3962.

(14) Maia, L. B.; Moura, J. J. G. How Biology Handles Nitrite. *Chem. Rev.* **2014**, *114* (10), 5273−5357.

(15) Stroupe, M. E.; Getzoff, E. D., The Role of Siroheme in Sulfite and Nitrite Reductases. *Tetrapyrroles. Molecular Biology Intelligence Unit*; Springer: New York, 2009.

(16) Crane, B. R.; Getzoff, E. D. The relationship between structure and function for the sulfite reductases. *Curr. Opin. Struct. Biol.* **1996**, *6* (6), 744−756.

(17) Crane, B. R.; Siegel, L. M.; Getzoff, E. D. Sulfite Reductase Structure at 1.6 Å: Evolution and Catalysis for Reduction of Inorganic Anions. *Science* **1995**, *270* (5233), 59.

(18) Allen, J. W.; Ferguson, S. J.; Fülöp, V. Cytochrome cd1 Nitrite Reductase. In *Encyclopedia of Inorganic and Bioinorganic Chemistry*; Scott, R. A., Ed.; Wiley Online Library, 2011.

(19) Dailey, H. A.; Dailey, T. A.; Gerdes, S.; Jahn, D.; Jahn, M.; O'Brian, M. R.; Warren, M. J. Prokaryotic Heme Biosynthesis: Multiple Pathways to a Common Essential Product. *Microbiol. Mol. Biol. Rev.* **2017**, *81* (1), XXX.

(20) Murshudov, G. N.; Grebenko, A. I.; Barynin, V.; Dauter, Z.; Wilson, K. S.; Vainshtein, B. K.; Melik-Adamyan, W.; Bravo, J.; Ferrán, J. M.; Ferrer, J. C.; Switala, J.; Loewen, P. C.; Fita, I. Structure of the Heme d of Penicillium vitale and Escherichia coli Catalases. *J. Biol. Chem.* **1996**, *271* (15), 8863−8868.

(21) Obinger, C.; Maj, M.; Nicholls, P.; Loewen, P. Activity, Peroxide Compound Formation, and Heme d Synthesis inEscherichia coliHPII Catalase. *Arch. Biochem. Biophys.* **1997**, *342* (1), 58−67.

(22) Timkovich, R.; Cork, M. S.; Gennis, R. B.; Johnson, P. Y. Proposed structure of heme d, a prosthetic group of bacterial terminal oxidases. *J. Am. Chem. Soc.* **1985**, *107* (21), 6069−6075.

(23) Bhagi-Damodaran, A.; Petrik, I. D.; Marshall, N. M.; Robinson, H.; Lu, Y. Systematic Tuning of Heme Redox Potentials and Its Effects on O2 Reduction Rates in a Designed Oxidase in Myoglobin. *J. Am. Chem. Soc.* **2014**, *136* (34), 11882−11885.

(24) Richardson, P. F.; Chang, C. K.; Spaulding, L. D.; Fajer, J. Radicals of isobacteriochlorins: models of siroheme and sirohydrochlorin. *J. Am. Chem. Soc.* **1979**, *101* (26), 7736−7738.

(25) Sullivan, E. P.; Grantham, J. D.; Thomas, C. S.; Strauss, S. H. Proton NMR study of high-spin iron(III) isobacteriochlorins. The effects of five- vs six-coordination and comparisons with homologous porphyrin and chlorin complexes. *J. Am. Chem. Soc.* **1991**, *113*, 5264.

(26) Richardson, P. F.; Chang, C. K.; Hanson, L. K.; Spaulding, L. D.; Fajer, J. Cation radicals of isobacteriochlorins. Implications for nitrite and sulfite reductases. *J. Phys. Chem.* **1979**, *83* (26), 3420−3424.

(27) Chang, C. K. Synthesis and characterization of alkylated isobacteriochlorins, models of siroheme and sirohydrochlorin. *Biochemistry* **1980**, *19* (9), 1971−1976.

(28) Stolzenberg, A. M.; Spreer, L. O.; Holm, R. H. Iron octaethylisobacteriochlorin, a model system for the siroheme prosthetic group of nitrite and sulphite reductases. *J. Chem. Soc., Chem. Commun.* **1979**, No. 23, 1077−1078.

(29) Stolzenberg, A. M.; Strauss, S. H.; Holm, R. H. Iron(II, III)-chlorin and -isobacteriochlorin complexes. Models of the heme prosthetic groups in nitrite and sulfite reductases: means of formation and spectroscopic and redox properties. *J. Am. Chem. Soc.* **1981**, *103* (16), 4763−4778.

(30) Stolzenberg, A. M.; Spreer, L. O.; Holm, R. H. Octaethylisobacteriochlorin, a model of the sirohydrochlorin ring system of siroheme enzymes: preparation and spectroscopic and electrochemical properties of the free base and its zinc(II) complex. *J. Am. Chem. Soc.* **1980**, *102* (1), 364−370.

(31) Zhou, C.; Cai, L.; Holm, R. H. Synthesis of a [Fe4S4]−S−Ferriheme Bridged Assembly Containing an Isobacteriochlorin Component: A Further Analogue of the Active Site of Sulfite Reductase. *Inorg. Chem.* **1996**, *35* (10), 2767−2772.

(32) Wei, Z.; Ryan, M. D. Infrared Spectroelectrochemical Reduction of Iron Porphyrin Complexes. *Inorg. Chem.* **2010**, *49* (15), 6948−6954.

(33) Mase, K.; Yoneda, M.; Yamada, Y.; Fukuzumi, S. Seawater usable for production and consumption of hydrogen peroxide as a solar fuel. *Nat. Commun.* **2016**, *7*, 11470.

(34) Mase, K.; Ohkubo, K.; Fukuzumi, S. Much Enhanced Catalytic Reactivity of Cobalt Chlorin Derivatives on Two-Electron Reduction

DOI: 10.1021/acs.inorgchem.8b02063
Inorg. Chem. XXXX, XXX, XXX−XXX

of Dioxygen to Produce Hydrogen Peroxide. *Inorg. Chem.* **2015**, *54* (4), 1808−1815.
(35) Maher, A. G.; Passard, G.; Dogutan, D. K.; Halbach, R. L.; Anderson, B. L.; Gagliardi, C. J.; Taniguchi, M.; Lindsey, J. S.; Nocera, D. G. Hydrogen Evolution Catalysis by a Sparsely Substituted Cobalt Chlorin. *ACS Catal.* **2017**, *7* (5), 3597−3606.
(36) Schweyen, P.; Hoffmann, M.; Krumsieck, J.; Wolfram, B.; Xie, X.; Bröring, M. Metal-Assisted One-Pot Synthesis of Isoporphyrin Complexes. *Angew. Chem., Int. Ed.* **2016**, *55* (34), 10118−10121.
(37) Fujii, H.; Yamaki, D.; Ogura, T.; Hada, M. The functional role of the structure of the dioxo-isobacteriochlorin in the catalytic site of cytochrome cd1 for the reduction of nitrite. *Chemical Science* **2016**, *7* (4), 2896−2906.
(38) Mase, K.; Ohkubo, K.; Fukuzumi, S. Efficient Two-Electron Reduction of Dioxygen to Hydrogen Peroxide with One-Electron Reductants with a Small Overpotential Catalyzed by a Cobalt Chlorin Complex. *J. Am. Chem. Soc.* **2013**, *135* (7), 2800−2808.
(39) Sheldrick, G. *SHELXL97, Program for Crystal Structure Refinement from Diffraction Data*; University of Göttingen: Göttingen, Germany, 1997.
(40) Sheldrick, G. *SHELXS97: Program for the Solution of Crystal Structure*; University of Göttingen: Göttingen, Germany, 1997.
(41) Spek, A. Single-crystal structure validation with the program PLATON. *J. Appl. Crystallogr.* **2003**, *36* (1), 7−13.
(42) Farrugia, L. ORTEP-3 for Windows - a version of ORTEP-III with a Graphical User Interface (GUI). *J. Appl. Crystallogr.* **1997**, *30*, 565.
(43) Farrugia, L. WinGX suite for small-molecule single-crystal crystallography. *J. Appl. Crystallogr.* **1999**, *32* (4), 837−838.
(44) Amanullah, S.; Das, P. K.; Samanta, S.; Dey, A. Tuning the thermodynamic onset potential of electrocatalytic O2 reduction reaction by synthetic iron-porphyrin complexes. *Chem. Commun.* **2015**, *51* (49), 10010−10013.
(45) Gałęzowski, M.; Gryko, D. T. Synthesis of Locked meso-*β*-Substituted Chlorins via 1,3-Dipolar Cycloaddition. *J. Org. Chem.* **2006**, *71* (16), 5942−5950.
(46) Adler, A. D.; Longo, F. R.; Finarelli, J. D.; Goldmacher, J.; Assour, J.; Korsakoff, L. A simplified synthesis for meso-tetraphenylporphine. *J. Org. Chem.* **1967**, *32* (2), 476−476.
(47) Connelly, N. G.; Draggett, P. T.; Green, M.; Kuc, T. A. Synthesis and reactivity of the tetrakis(acetonitrile)nitrosylrhodium dication. *J. Chem. Soc., Dalton Trans.* **1977**, No. 1, 70−73.
(48) Harrop, T. C.; Tonzetich, Z. J.; Reisner, E.; Lippard, S. J. Reactions of Synthetic [2Fe-2S] and [4Fe-4S] Clusters with Nitric Oxide and Nitrosothiols. *J. Am. Chem. Soc.* **2008**, *130* (46), 15602−15610.
(49) Frisch, M. J. T. e. a. *Gaussian 03*, version C.02; Gaussian, Inc.: Wallingford, CT, 2004.
(50) Krishnan, R.; Binkley, J. S.; Seeger, R.; Pople, J. A. Self-consistent molecular orbital methods. XX. A basis set for correlated wave functions. *J. Chem. Phys.* **1980**, *72* (1), 650−654.
(51) McLean, A. D.; Chandler, G. S. Contracted Gaussian basis sets for molecular calculations. I. Second row atoms, Z = 11−18. *J. Chem. Phys.* **1980**, *72* (10), 5639−5648.
(52) Tenderholt, A. L. *QMForge*, version 2.4.
(53) Cossi, M.; Rega, N.; Scalmani, G.; Barone, V. Energies, structures, and electronic properties of molecules in solution with the C-PCM solvation model. *J. Comput. Chem.* **2003**, *24* (6), 669−681.
(54) Reiss, H.; Heller, A. The absolute potential of the standard hydrogen electrode: a new estimate. *J. Phys. Chem.* **1985**, *89* (20), 4207−4213.
(55) Sligar, S. G. Coupling of spin, substrate, and redox equilibriums in cytochrome P450. *Biochemistry* **1976**, *15* (24), 5399−5406.
(56) Martin, F.; Zipse, H. Charge distribution in the water molecule—A comparison of methods. *J. Comput. Chem.* **2005**, *26* (1), 97−105.
(57) McQuarters, A. B.; Kampf, J. W.; Alp, E. E.; Hu, M.; Zhao, J.; Lehnert, N. Ferric Heme-Nitrosyl Complexes: Kinetically Robust or Unstable Intermediates? *Inorg. Chem.* **2017**, *56* (17), 10513−10528.
(58) Praneeth, V. K. K.; Näther, C.; Peters, G.; Lehnert, N. Spectroscopic Properties and Electronic Structure of Five- and Six-Coordinate Iron(II) Porphyrin NO Complexes: Effect of the Axial N-Donor Ligand. *Inorg. Chem.* **2006**, *45* (7), 2795−2811.
(59) Rinaldo, S.; Arcovito, A.; Brunori, M.; Cutruzzolà, F. Fast Dissociation of Nitric Oxide from Ferrous Pseudomonas aeruginosa cd1 Nitrite Reductase: A NOVEL OUTLOOK ON THE CATALYTIC MECHANISM. *J. Biol. Chem.* **2007**, *282* (20), 14761−14767.

DOI: 10.1021/acs.inorgchem.8b02063
Inorg. Chem. XXXX, XXX, XXX−XXX